

**PSFC/JA-07-24**

**Microturbulent drift mode suppression  
as a trigger mechanism for internal transport  
barriers on Alcator C-Mod**

K. Zhurovich, C. L. Fiore, D. R. Ernst, P. T. Bonoli,  
M. J. Greenwald, A. E. Hubbard, J. W. Hughes,  
E. S. Marmor, D. R. Mikkelsen<sup>†</sup>, P. Phillips<sup>§</sup> and J. E. Rice

<sup>†</sup>*Princeton Plasma Physics Laboratory, Princeton, New Jersey 08543*

<sup>§</sup>*Fusion Research Center, University of Texas, Austin, Texas 78712*

Written in 2007, published in 2010

**Plasma Science and Fusion Center  
Massachusetts Institute of Technology  
Cambridge MA 02139 USA**

This work was supported by the U.S. Department of Energy, Grant No. US-DoE DE-FC02-99ER54512. Reproduction, translation, publication, use and disposal, in whole or in part, by or for the United States government is permitted.

# Microturbulent drift mode suppression as a trigger mechanism for internal transport barriers on Alcator C-Mod.

K. Zhurovich, C. L. Fiore, D. R. Ernst, P. T. Bonoli, M. J. Greenwald, A. E. Hubbard, J. W. Hughes, E. S. Marmor, D. R. Mikkelsen<sup>†</sup>, P. Phillips<sup>§</sup> and J. E. Rice

*Plasma Science and Fusion Center, Massachusetts Institute of Technology, Cambridge, Massachusetts 02139*

*<sup>†</sup>Princeton Plasma Physics Laboratory, Princeton, New Jersey 08543*

*<sup>§</sup>Fusion Research Center, University of Texas, Austin, Texas 78712*

Internal transport barriers (ITBs) can be routinely produced in enhanced  $D_\alpha$  (EDA) H-mode discharges on the Alcator C-Mod tokamak by putting the minority ion cyclotron resonance layer at  $|r/a| \geq 0.5$  during the current flat top phase of the discharge. These ITBs are characterized by density peaking at constant temperature, and are therefore both particle and energy transport barriers. The ITB formation appears to result from widening the region near the magnetic axis in which toroidal drift modes are stable, allowing the Ware pinch to peak the density profile. Experimental evidence shows that shifting the ICRF resonance off axis results in a local flattening of ion and electron temperature profiles. TRANSP calculations of ion temperature profiles support this experimentally observed trend. Stability analysis of ion temperature gradient (ITG) and electron temperature gradient (ETG) modes at times before ITB formation is done using the linear gyrokinetic code GS2. These gyrokinetic calculations find that the most unstable modes in the C-Mod EDA H-mode core, prior to ITB onset, are the toroidal ion temperature gradient driven type. These modes are suppressed in the ITB region through a temperature gradient reduction when the ICRF resonance is shifted off axis.

## 1. Introduction.

Internal transport barriers (ITBs) in tokamak plasmas are characterized by the reduction of transport in one or more of the particle, momentum, or energy channels in the core plasma region. Most ITBs on the Alcator C-Mod tokamak are produced in a double transport barrier regime, where an internal transport barrier is formed in the presence of the edge high confinement mode (H-mode) pedestal [1-4]. In this paper we investigate the stabilization mechanism for triggering ITBs by heating in the ion cyclotron range of frequencies (ICRF). These ITBs can be routinely produced in C-Mod steady enhanced  $D_\alpha$  (EDA) H-mode plasmas by applying off-axis ( $|r/a| \geq 0.5$ ) ICRF heating on either the high or low field side. They are observed primarily in the electron particle channel and are marked by the steepening of the density and pressure profile following the L-H transition. The fact that the central temperature does not decrease as the density rises is evidence that a thermal barrier exists as well [3, 4]. Further evidence of a thermal barrier is seen in the delay of the propagation of the sawtooth heat pulse crash across the barrier region [3]. Peaked density profiles are desirable for steady-state tokamak operation and especially for the advanced tokamak studies because of the bootstrap current, which is generated as a consequence of the steep pressure gradient formed by the ITB. Since bootstrap current drive depends more strongly on the density gradient than on the temperature gradient, peaked density is a favorable regime for a reactor operation. Peaked density profiles also provide better fusion yield and ITBs are considered as one of the ITER “hybrid” scenarios. Of course, the major drawback of density peaking is the possible increase in core impurity accumulation. However, previous results [4-6] on C-Mod showed that addition of on-axis ICRF heating into the center after the barrier has formed arrests both further density peaking and impurity accumulation.

There is evidence on other tokamaks that links various types of ITB formation to the  $\overline{E} \times \overline{B}$  shearing rate (proportional to the rotation velocity gradient) exceeding the maximum

growth rate for ion temperature gradient (ITG) driven turbulence [7-9]. Several experiments have produced ITBs by using high power neutral beam injection, sometimes complemented by auxiliary ICRF power or lower hybrid current drive, applied during the plasma current rise phase [10-14]. This leads to low or reversed magnetic shear in the core plasma region with the ITB foot located near the position of minimum  $q$  value. The connection between ITB formation and plasma rotation in plasmas with neutral beam injection is obscured by the inherent sources of particles and momentum.

ICRF heated ITBs on the C-Mod tokamak are produced in the absence of neutral beam injection, and therefore, with no external momentum input or central fueling. They are compatible with H-mode edge and can be run in a steady-state mode [15]. Ions and electrons are well equilibrated in C-Mod H-mode plasmas due to high density. All of these factors make this regime relevant for reactor type scenarios.

The location of these ITBs can be somewhat controlled through the  $q$  profile with higher  $q_{95}$  values leading to the narrow ITBs [6, 16]. The typical ITB location lies between  $q$  values of 1.1 and 1.34. So far the location and the triggering of the ITBs on C-Mod have not been linked to any particular rational  $q$  surfaces. Most of the ITB discharges on C-Mod have sawtooth oscillations with the inversion radius well inside the ITB foot, which means  $q_0 < 1$ . Since these ITBs are formed during the current flat top phase, it means the  $q$  profile is monotonic and therefore, these plasmas lack the reversed magnetic shear stabilization mechanism present on other machines. Measurements of plasma flows on C-Mod are too limited to make conclusive statements about the role of the flow shear stabilization. However, it is estimated [5] that the  $\overline{E} \times \overline{B}$  shearing rate is not significant on C-Mod during the late phase of the ITB, but its role during formation is unclear.

Suppression of toroidal ITG modes in the ITB region may explain access to the off-axis ICRF heated ITBs. For a given ICRF frequency, the condition of achieving ICRF heated ITBs in C-Mod plasmas strongly depends on the magnetic field with small (if any) hysteresis

[1, 4]. Given the one-to-one relation between ICRF frequency, the magnetic field, and thus the ICRF power deposition profile, this fact in turn suggests a strong dependence on the RF resonance location. Moving the RF resonance outward can locally flatten the temperature profiles and reduce the drive for ITG and electron temperature gradient (ETG) driven modes. Plasma conditions in the core ITB region are close to marginal stability [17], so that even a small flattening can lead to a significant drop in the turbulence level. Redi *et al.* [18] performed microturbulent drift mode stability analyses of the C-Mod H-mode plasmas, supporting a link between turbulence suppression and ITB formation. It has been demonstrated experimentally that small amounts of on-axis ICRF can halt the density rise, allowing control of the ITB [4, 6]. The mechanism for this control has been explored through nonlinear gyrokinetic simulations and comparison fluctuation measurements [5, 17, 19], and is linked to the temperature dependent excitation of trapped electron mode (TEM) turbulence driven by the density gradient. This paper investigates the triggering mechanism for the ICRF heated ITBs on C-Mod in more detail and provides new results from experiments dedicated to this study, gyrokinetic stability analysis, and new results of transport analysis.

In the following, we provide a description of the experimental setup in Sec. 2 and present experimental measurements of the temperature gradients in Sec. 3. The results of TRANSP modeling of representative discharges are discussed in Sec. 4, while the results of gyrokinetic stability calculations are presented in Sec. 5. We conclude the paper with a summary of the results in Sec. 6.

## **2. Experimental setup and diagnostics.**

Alcator C-Mod is a compact (major radius  $R=0.67$  m, typical minor radius  $a=0.21$  m) high field ( $2.6 \text{ T} < B_T < 8.1 \text{ T}$ ) diverted tokamak [20]. The discharges analyzed here have a single lower null, which corresponds to standard operation. The plasma facing components consist of molybdenum tiles, which are usually coated with boron shortly before ITB-related

experiments. The operating range for such experiments includes plasma current up to 1.5 MA and line-averaged electron density up to  $4 \times 10^{20} \text{ m}^{-3}$  during the pre-ITB phase of a discharge. In addition to Ohmic heating, C-Mod uses auxiliary ICRF D(H) (minority in parentheses) minority heating power, coupled to the plasma through three (2 two-strap and 1 four-strap) fast wave antennas operated in heating phasing. The two-strap antennas operate at fixed 80 MHz frequency and together deliver up to 3 MW [21]. The four-strap antenna can be set to operate at 50, 70, or 78 MHz, delivering up to 3 MW [22]; experiments described here used 70 and 78 MHz setups. 5.4 T operation corresponds to the ICRF resonance location being at  $r/a \sim 0.5$  (on the low field side) for 70 MHz and  $r/a \sim 0.15$  for 80 MHz. For 4.5 T discharges the ICRF resonance is located at  $r/a \sim 0.15$  for 70 MHz and at  $r/a \sim 0.5$  (high field side) for 80 MHz respectively. The convention is such that the resonance location at  $|r/a| < 0.2$  is considered on-axis heating, or central, heating, while  $|r/a| > 0.2$  is considered off-axis heating, although ITBs are typically not triggered until the resonance location is  $|r/a| \geq 0.5$ .

Electron temperature ( $T_e$ ) on C-Mod is measured using a variety of diagnostics. These include two grating polychromator (GPC) electron cyclotron emission (ECE) systems, one with 9 and the other with 18 spatial channels [23, 24], and a heterodyne 32-channel ECE system [25]. These are complemented by the measurements from the Thomson scattering (TS) systems [26, 27]. Electron density ( $n_e$ ) is measured by TS and a multi-chord two-color interferometer (TCI) [28]. The visible Bremsstrahlung diagnostic on C-Mod [29] detects continuum emission from the plasma and yields the profile of  $n_e \sqrt{Z_{eff}}$ . These measurements combined with TS density profiles enable us to derive profiles of  $Z_{eff}$ . A limited amount of ion temperature ( $T_i$ ) profile data is obtained from a scannable array of five high spectral resolution x-ray spectrometers (HIREX) [30]. Spectra from Ar emission are typically collected every 50-100 ms during plasma discharges, and averaged over the sawtooth oscillations which are normally present. The total neutron flux is measured using

two different systems. The first one consists of 18 neutron detectors, has 1 msec time resolution, and is absolutely calibrated with  $\text{Cf}^{252}$  and D-D fusion neutrons from Alcator C-Mod [31]. The second detector system provides fast measurements of the total neutron production with 0.1 msec time resolution and is cross-calibrated with the first system. Measured neutron rate, due its high sensitivity to the ion temperature, enables us to determine the central value of the ion temperature.

### 3. Experimental observations.

The observed cross-field transport of particles and energy in high temperature fusion plasmas usually exceeds values predicted by neoclassical theory and is widely associated with the turbulence caused by drift modes [32]. ITG and ETG modes are believed to play an important role in plasma confinement and ITB formation. These modes become unstable if  $\eta_{i,e} > \eta_{\text{crit}}$ , where  $\eta_{i,e} = L_n/L_T$  for ions or electrons correspondingly. In the flat density limit,  $L_n \gg L_T$ , this criterion becomes a criterion on  $R/L_T$  rather than on  $\eta$ , and  $R/L_T > R/L_{T\text{crit}}$  for instability [33].

ICRF heated ITBs on C-Mod are formed in steady-state EDA H-modes, which have relatively flat density profiles. Our hypothesis is that putting the ICRF resonance position off-axis flattens the temperature profiles, reducing the driving mechanism for the temperature gradient driven modes over considerable plasma volume. During standard steady-state EDA H-mode operation, the inward particle Ware pinch is believed to be balanced or dominated by the outward diffusion, resulting in a flat density profile. Fig. 1(a) depicts a typical density profile during the steady-state H-mode phase. Circles and squares represent TS measurements from the core and edge systems, respectively. The solid line shows the fit to the data. Reducing the drive for the temperature gradient driven modes can suppress the outward diffusion. This can shift the balance in favor of the inward particle pinch and result in ITB

formation and density profile peaking even without  $\overline{E} \times \overline{B}$  shear effects. Ernst *et al.* [17] previously estimated through non-linear gyrokinetic simulations that the Ware pinch on C-Mod is sufficient to account for the observed density peaking. Fig. 1(b) shows the electron density profile in the fully developed ITB phase. The ITB is clearly distinguished with its foot located near  $R = 0.8$  m, while the edge pedestal in this double barrier regime is located near  $R = 0.89$  m. Vertical bars at  $R = .74$  m,  $0.76$  m,  $0.78$  m,  $0.80$  m,  $0.82$  m, and  $0.84$  m in Fig. 1(b) represent some radial locations of interest around the ITB foot location.

The working hypothesis is simply that broadening the temperature profile with off-axis ICRH suppresses toroidal ITG modes, allowing neoclassical particle pinch to peak the density profile. Several sets of experiments were done on the C-Mod tokamak to test this idea. During the first set of experiments the toroidal magnetic field was varied between discharges from 5.45 T to 6.27 T, thus moving the ICRF resonance radially outward. In order

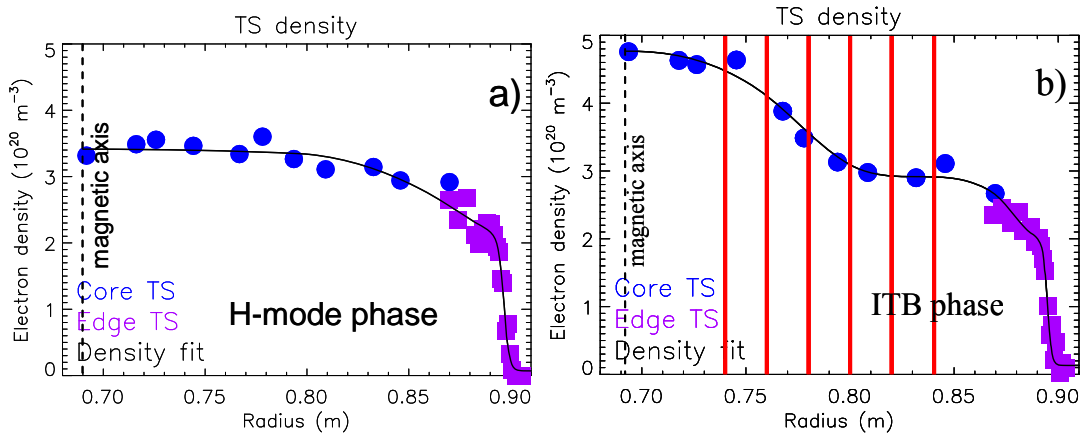


Figure 1(Color online).

Typical plasma density profiles during a) steady-state H-mode phase and b) fully developed ITB phase. Circles and squares represent experimental measurements from the core and edge Thomson scattering diagnostics respectively, while solid line shows a fit to the experimental data. The error bars on the Thomson data are around 10%. ITB foot is located at around  $R = 0.8$  m, or  $r/a = 0.5$ . Vertical lines represent regions of interest for the temperature gradient analysis.

to minimize other stabilizing effects, the total RF power was kept constant and the total plasma current was adjusted proportionally to the magnetic field (from 0.86 MA to 1 MA) to



keep the safety factor  $q$  profile unchanged at  $q_{95} = 4.5$ . The ICRF antennas operated at 80 MHz, therefore the magnetic field scan resulted in a scan of the ICRF resonance position on the low field side. Figure 2 shows some of the plasma parameters for two representative discharges from this scan: a non-ITB (a) and an ITB (b) discharge. With the application of 2.8 MW of ICRF power at 0.6 s, the plasma immediately undergoes a transition from L-mode to EDA H-mode. In the discharge that does not develop an ITB, the density profile remains flat as can be judged by the density peaking ratio, while for the ITB discharge the density

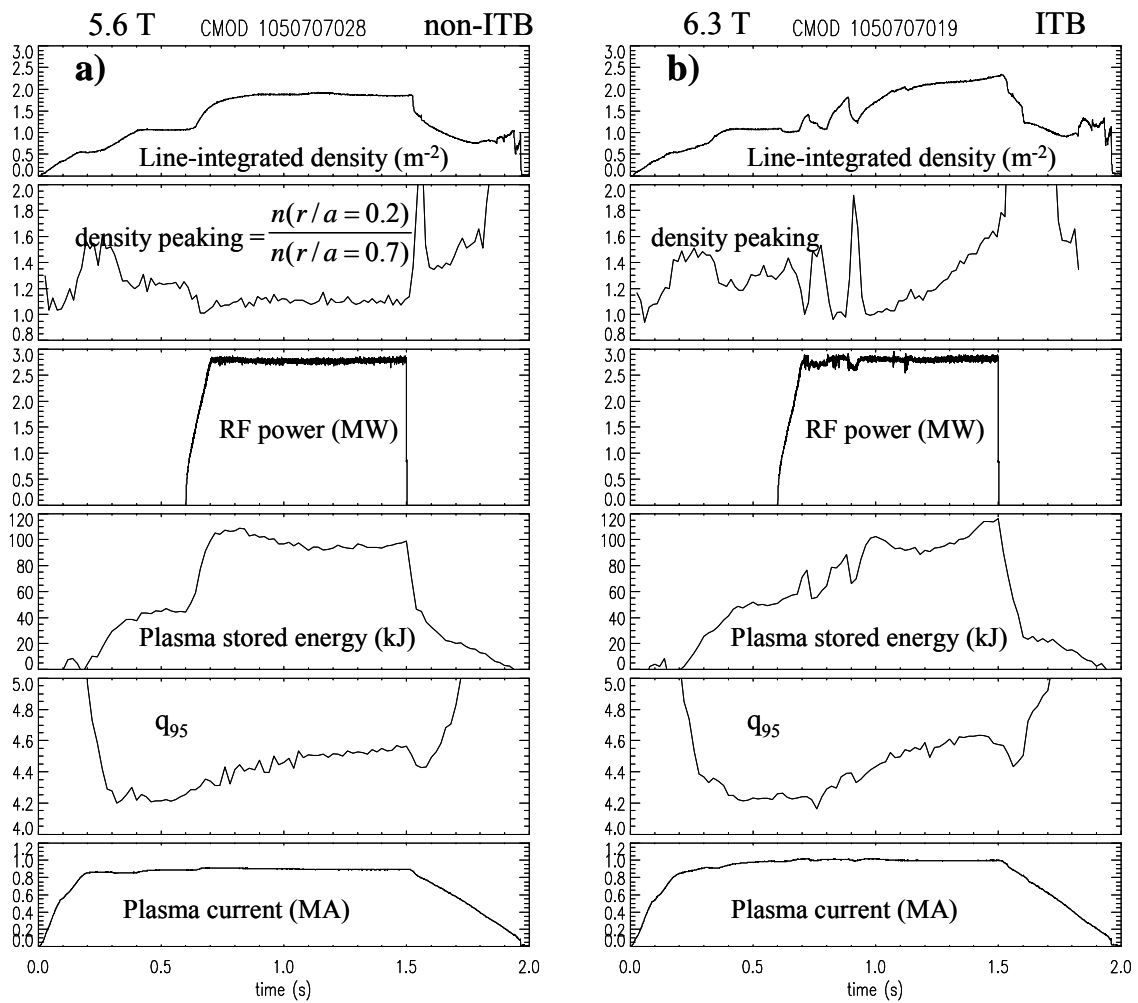


Figure 2.

Selected plasma parameters for two representative discharges: non-ITB (a) and ITB (b), from the magnetic field scan experiment. During these experiments total ICRF power was kept constant and plasma current was adjusted proportionally to the magnetic field to keep  $q_{95}$  constant. Both discharges undergo L-H transition with an application of RF power. (a) Lower field translates

into on-axis heating with the ICRF resonance location at  $r/a = 0.15$ . Plasma remains in steady-state EDA H-mode regime. (b) Higher field results into more off-axis ICRF heating with the ICRF resonance location at  $r/a = 0.65$  and plasma develops an ITB.

peaking factor rises starting at 1.2-1.3 s. Some back transitions occur during the initial phase of the H-mode during the ITB discharge; however these are not associated with the ITB formation. A rise in plasma stored energy is also observed during the ITB phase. During the ITB phase the density is peaking in the core plasma region with the density profile during the fully developed ITB phase shown in Fig. 1(b).

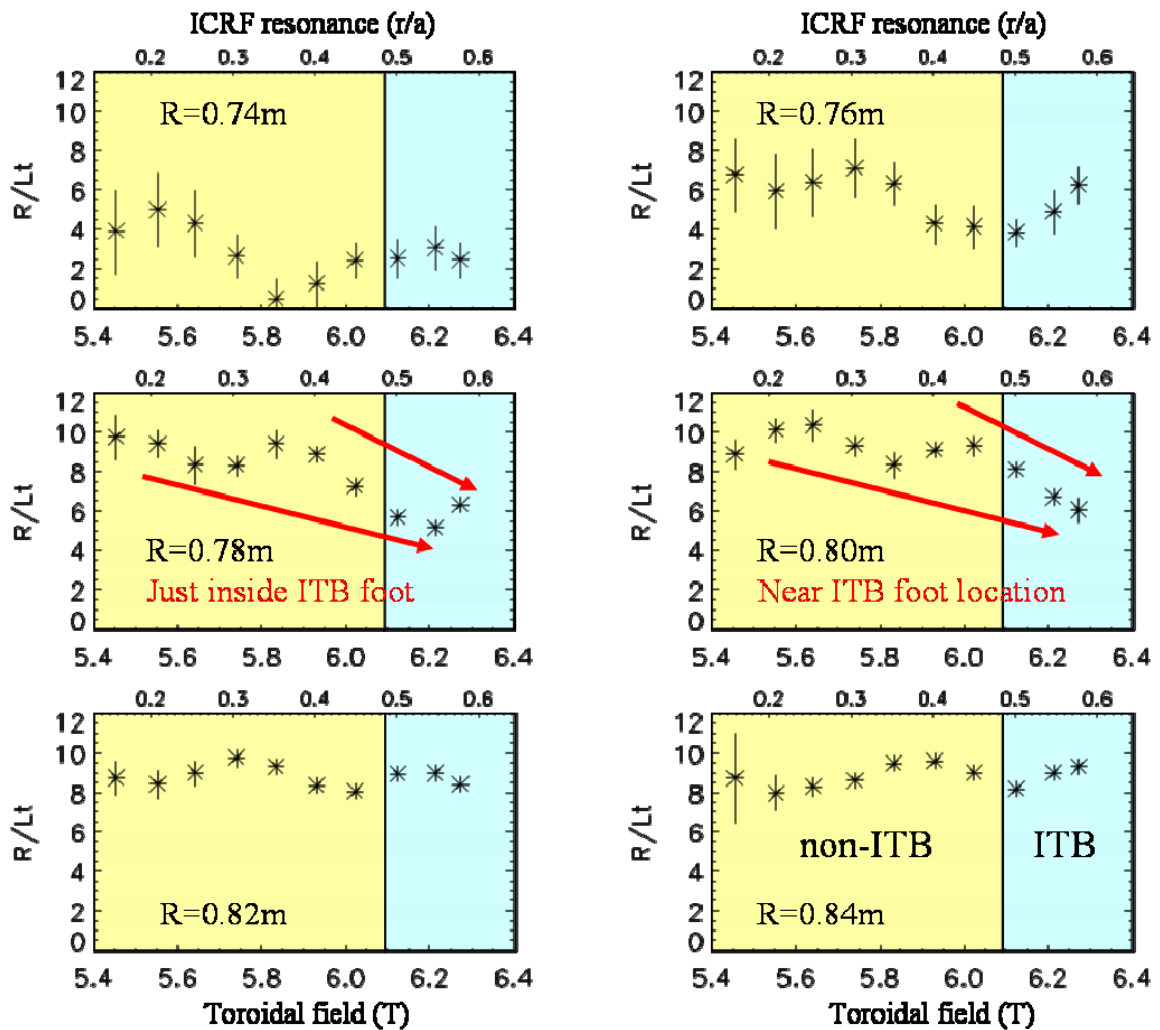


Figure 3 (Color online).

$R/L_T$  for the electron temperature calculated at the indicated radial positions shown on Fig. 1(b). Averaging has been done over steady portion during H-mode phase (pre-ITB for ITB discharges)

and therefore, over many sawtooth oscillations. The left region on each plot corresponds to non-ITB discharges, while the right region contains discharges that developed ITBs. For this experiment lower magnetic field translates into on-axis ICRF heating. The position of the ICRF resonance and therefore, the degree of “off-axis” heating is shown on the upper axis. While no systematic trend can be derived for inner or outer plasma regions, there is a downward trend for  $R/L_T$  at positions near or just inside ITB foot location as shown by the arrows.

In order to examine how the shift of the ICRF resonance location affects the temperature profiles, the inverse electron temperature scale lengths ( $L_T^{-1} = \frac{1}{T} \frac{dT}{dr}$ ) were calculated at the radial locations marked in Fig. 1(b). The results of this analysis are shown in Fig. 3. The electron temperature profiles were measured by the C-Mod 9-channel GPC ECE system. The averaging of the gradient was done over steady portions of the discharges during the H-mode (pre-ITB for ITB cases) phase and therefore, over many sawteeth periods. Since it is difficult to compare temperature gradients for discharges which differ by 0.1-0.2 T but are otherwise similar, the goal is to look for a systematic trend with the magnetic field. Change in the magnetic field changes the ICRF resonance position, which is shown on the upper axis of each plot. No trend for  $R/L_T$  can be inferred for the inner or outer radial chords. On the contrary, the analysis of the temperature scale lengths at radial positions near or just inside the ITB foot suggests that there is a decrease in  $R/L_T$  for discharges that develop ITBs compared to non-ITB discharges. The pre-ITB values of  $R/L_T$  for ITB discharges at these radial positions are systematically lower than those from all non-ITB discharges.

Another set of experiments was done with an even more extensive toroidal magnetic field scan, where the magnetic field was varied from 3.7 T to 5.4 T on a discharge-by-discharge basis. With the ICRF system operating at 70 MHz, that resulted in the scan of the ICRF resonance location from the high to low field side,  $-0.5 \leq r/a \leq 0.5$ . For this set of discharges, some limited ion temperature profile information was available from the x-ray (HIREX) system with the central temperature derived from the neutron rate diagnostic. The results of these measurements are shown in Fig. 4. Circles correspond to the central ion

temperature as measured by the neutron rate system, whereas dots represent  $T_i(0)$  measurement from the HIREX system. From Fig. 4 one can tell that there is a good agreement between these two diagnostics. Asterisks depict off-axis ion temperature measurements done by the HIREX diagnostic at  $r/a = 0.3$ . Left and right regions correspond to the discharges which developed an ITB. The  $r/a$  position of the ICRF resonance in each case and therefore, the degree of “off-axis” heating is shown on the upper axis. For the discharges, where an ITB formed, the ICRF resonance position was at  $|r/a| \geq 0.5$  on HFS and LFS. The region in the middle contains data from the non-ITB discharges with the ICRF resonance location inside  $|r/a| = 0.5$ . From Fig. 4 it can be deduced that the difference between  $T_i(0)$  and  $T_i(0.3)$  is smaller for ITB discharges (side region) than it is for non-ITB discharges (central region). This observation suggests that the ion temperature profiles get flatter as the ICRF resonance location is moved off axis.

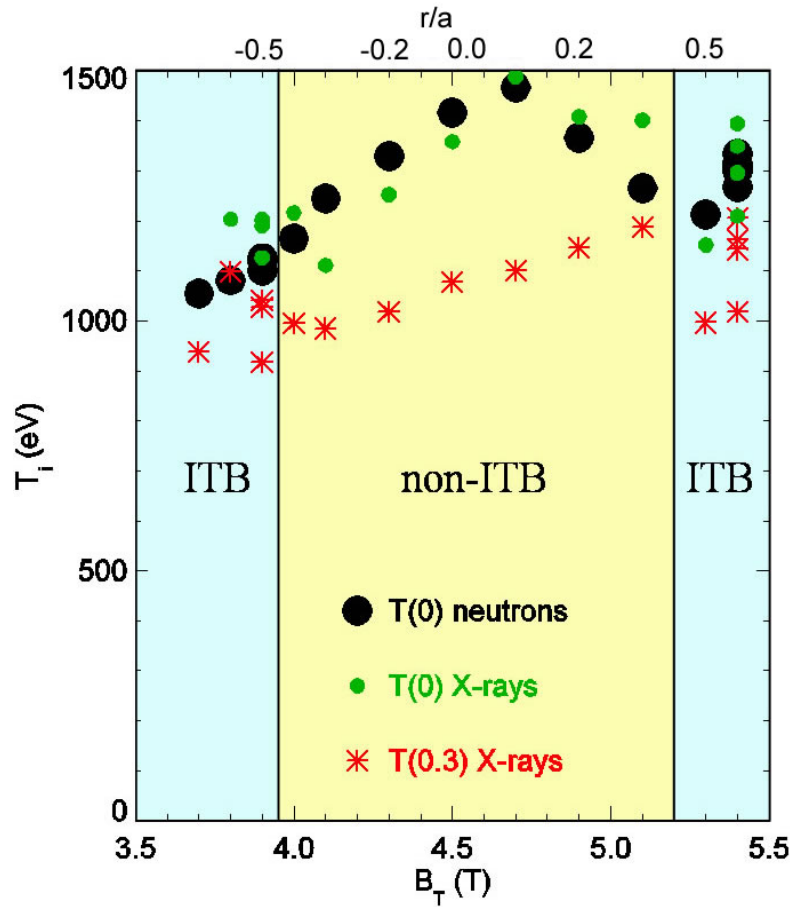


Figure 4 (Color online).

Ion temperature measurements. Circles are the central values of ion temperature derived from neutron rate measurements. Dots correspond to the central ion temperature as measured by x-ray (HIREX) diagnostic. Asterisks represent HIREX  $T_i$  measurements at  $r/a = 0.3$ . Central region corresponds to non-ITB discharges while left and right regions contain data from the discharges that developed ITBs. The position of the ICRF resonance and therefore, the degree of “off-axis” heating is shown on the upper axis. Since there is bigger gap between on- and off-axis  $T_i$  values for non-ITB discharges, this means that ion temperature profile gets flatter as the ICRF resonance is moved off-axis.

Finally a set of experiments was done where the ICRF setup was changed during a shot at a fixed toroidal magnetic field. These experiments were done with  $B_1=5.6$  T and therefore, 80 MHz operation corresponded to on-axis heating, while 70 MHz corresponded to off-axis LFS heating.

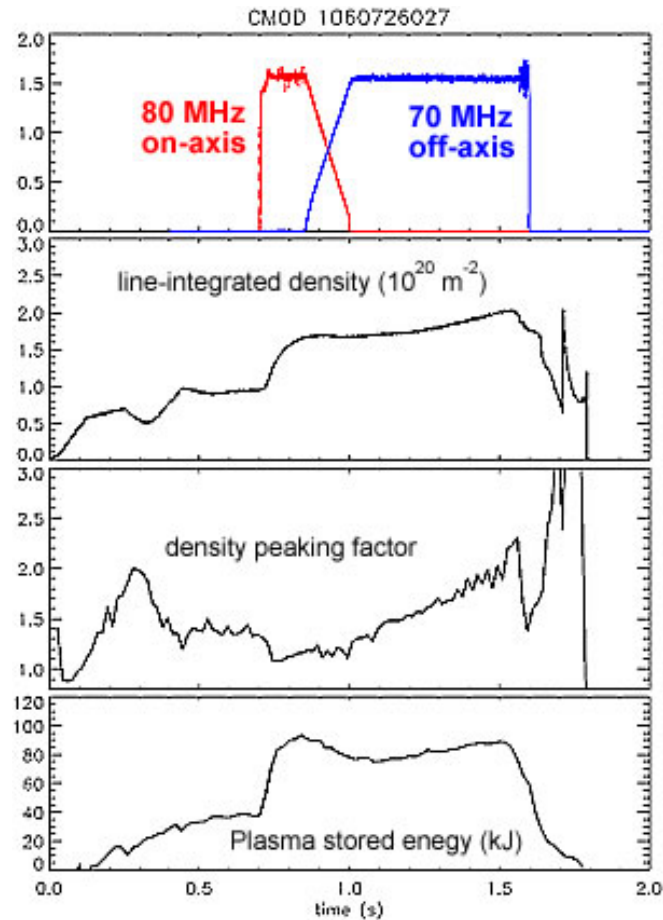
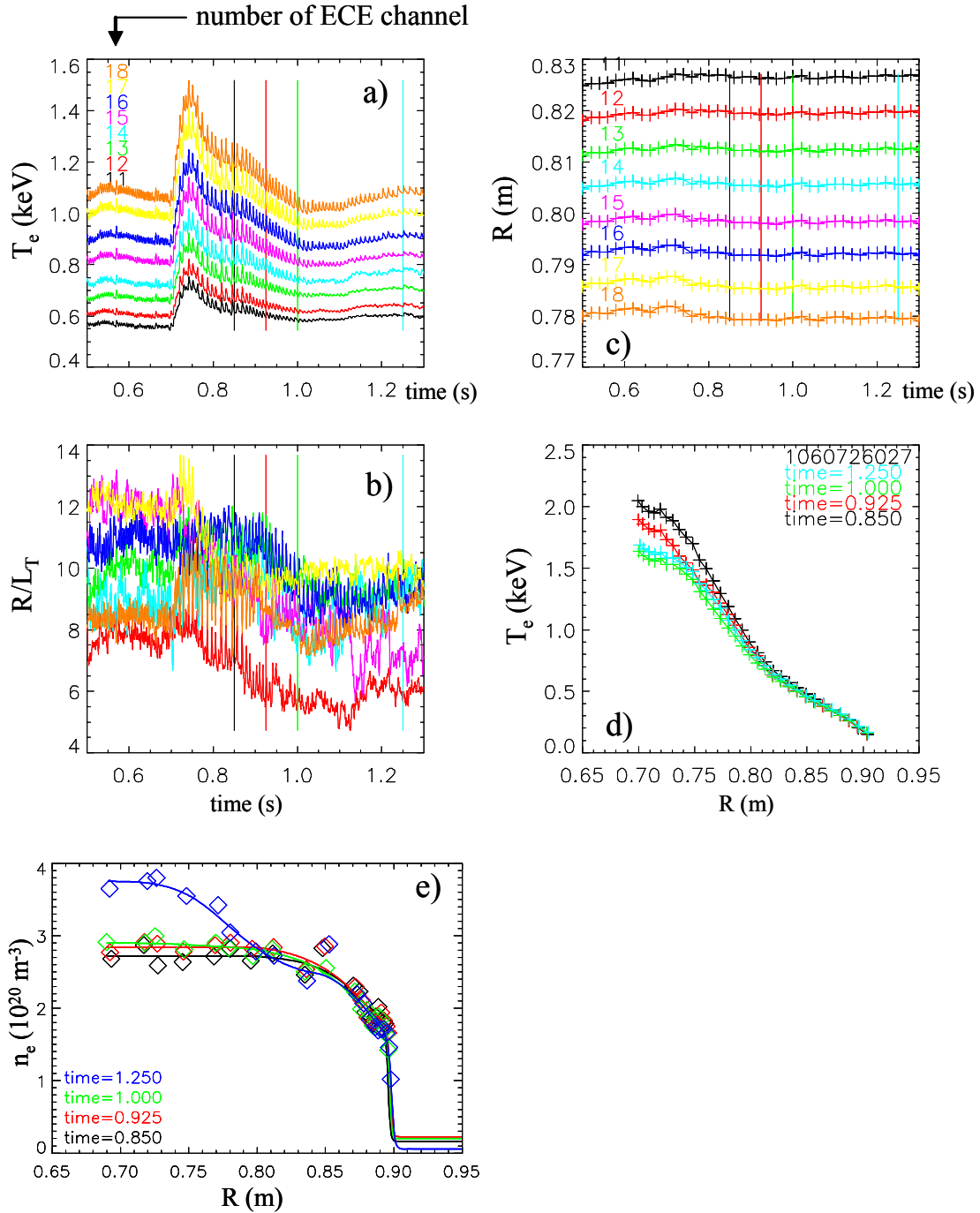


Figure 5 (Color online).

Selected plasma parameters for the selected discharges from the dual ICRF frequency setup experiment. Plasma undergoes L-H transition with the application of on-axis ICRF power, which 150 ms later is gradually traded over 150 ms time window for the off-axis RF power of the same magnitude. ITB develops during off-axis heating phase.

Some of the plasma parameters from a selected discharge are shown in Fig. 5. In this case the application of ICRF heating starts with the 80 MHz antenna, triggering an EDA H-mode. 150 ms into the H-mode phase of the discharge, the 80 MHz power is gradually traded over a 150 ms window for 70 MHz off-axis heating with the total ICRF power kept constant at 1.5 MW.



### Figure 6 (Color).

Electron temperature gradient measurements for the discharge in Fig. 5. (a) Electron temperature time traces of selected ECE channels. The channels are chosen around ITB foot with their radial position shown in Fig. 6(c). Vertical lines on plots (a) – (c) show time slices corresponding to 100% on-axis, 50%-50% on- and off-axis, and 100% off-axis heating phases (last two). (b)  $R/L_T$  values for selected radial ECE positions. This indicates that there is a decrease in  $R/L_T$  for radial positions around ITB foot as heating power is gradually shifted from on- to off-axis. (d) Electron temperature profile at selected times. Central temperature drops with no apparent change on the outer plasma region when the heating power is shifted outward. (e) Electron density profiles at selected times. ITB develops during the off-axis heating phase.

The rest of the discharge is continued with 100% off-axis heating. An ITB develops during this phase of the H-mode as can be seen on Fig. 5 from the rise of the line-integrated density, density peaking factor and the plasma stored energy. Electron temperature measurements were done using the heterodyne ECE system and the results of the measurements are presented in Fig. 6. Fig. 6(d) shows temperature profiles at times corresponding to 100% on-axis heating, 50%-50% on- and off-axis, and 100% off-axis heating (last two time slices). These times are marked by the vertical lines in the other panels. A reduction of the core temperature is observed when the heating scheme is changed from on-axis to off-axis. For a more careful analysis of the temperature gradient, several ECE radial channels are chosen around the ITB foot location. The ITB foot is located near  $R = 0.8$  m and the radial positions of the selected ECE channels are shown in Fig. 6(c). Temperature measurements as a function of time of the selected radial channels are shown in Fig. 6(a). Fig. 6(b) shows  $R/L_T$  corresponding to each of the selected ECE channels. From this plot it can be seen that  $R/L_T$  gradually decreases in the region of the ITB as the ICRF resonance is moved off axis. Electron density profiles at selected time slices are shown in Fig. 6(e). It is clearly seen that ITB develops during off-axis heating phase on a time scale of  $\sim 200$  ms.

#### 4. TRANSP modeling.

Measurements of ion temperature profiles on C-Mod are quite limited for most experiments. However, ion temperature profiles can be modeled by the transport analysis



code TRANSP [34], and such analysis was performed for the 80 MHz magnetic field scan. In these modeled discharges the plasma ion temperature profile was calculated under the assumption that  $\chi_i$  is proportional to the neoclassical ion thermal diffusivity [35],  $\chi_i = \kappa \chi_{\text{Hinton}}^{\text{Chang}}$ . The factor of proportionality  $\kappa$  is chosen in a feedback corrected loop such that the resultant calculated neutron rate matches the one measured in the experiment. The ICRF power deposition profile from the D(H) minority ion cyclotron heating is calculated by using the bounce-averaged Fokker Planck code coupled to the full wave code TORIC [36] integrated with TRANSP.

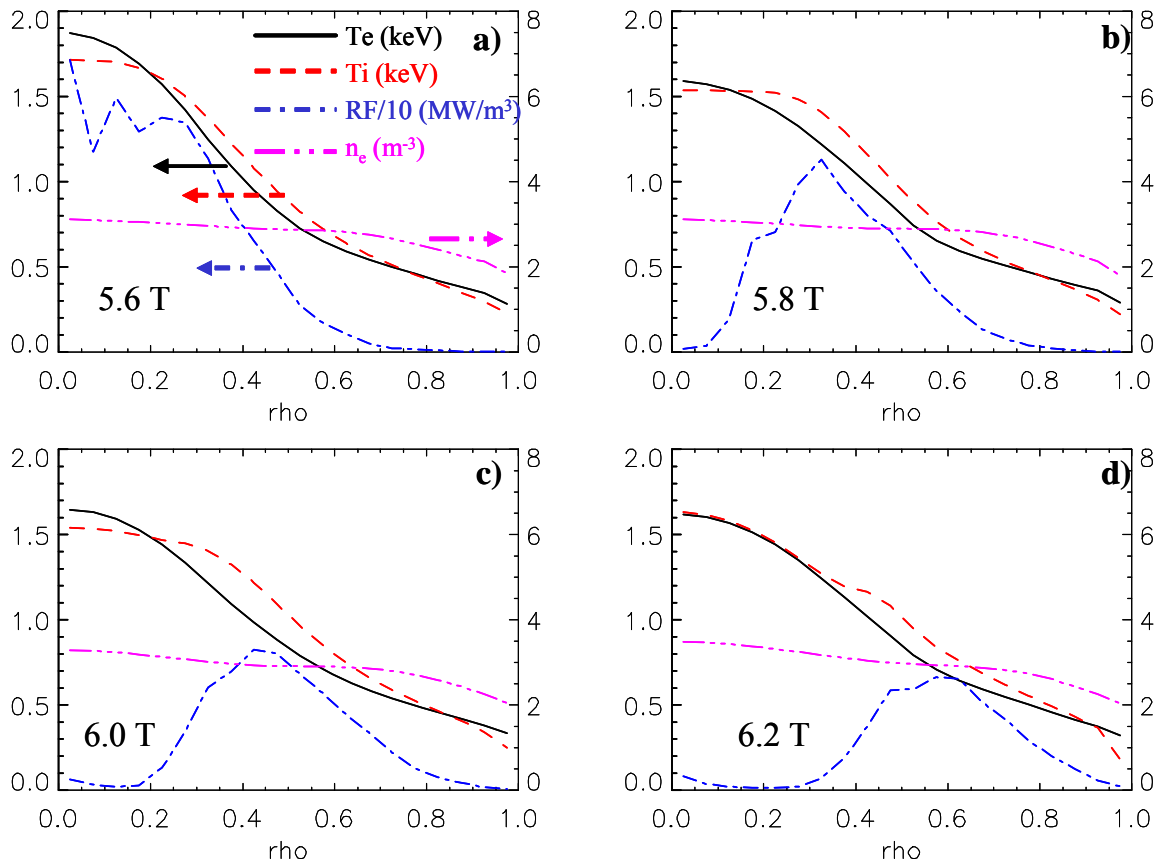


Figure 7 (Color online).

TRANSP calculations of ion temperature. Profiles are taken during H-mode (pre-ITB) phase of the discharges. Solid line - measured electron temperature; dashed line - calculated ion temperature; “— • —” - scaled ICRF power deposition profiles; “— • • • —” - measured electron density. Ion temperature profile flattens as the ICRF power deposition profile is moved outward, with the absolute deviation between  $T_i$  and  $T_e$  being small. The region of reduced  $T_i$  gradient moves with the ICRF resonance.

The results of this analysis are shown in Fig. 7. All of the calculated profiles are shown during the H-mode (pre-ITB) phase. Profiles are plotted against square root of normalized toroidal flux  $\rho = \sqrt{\psi}$ . Electron density profiles are similar for all discharges. Resultant ion temperature profiles (dashed line) are fairly close to the electron temperature (solid line), which is consistent with experimental observations and the fact that the high C-Mod density should lead to a strong coupling and therefore good equilibration between ions and electrons. The ion temperature profile measurements in this case were limited to the  $T_i(0)$  values derived from the neutron rate measurements. However, these values are in good agreement with both measured  $T_e(0)$  and TRANSP calculated  $T_i(0)$ . From Fig. 7 it can also be seen that changing the magnetic field indeed shifts the ICRF deposition profile. Furthermore, the modeled ion temperature profile gets broader as the ICRF resonance is moved outward, which is consistent with the experimental observations discussed previously. The discharge corresponding to Fig. 7(d) developed an ITB. The flat region of the ion temperature profile in this case shifts to  $r/a \sim 0.45$ , approximately the position where the ITB foot is seen later in the discharge. To illustrate further and quantify this trend, the values of  $R/L_T$  for the ion temperature profiles of Fig. 7 have been calculated at the radial positions shown in Fig. 1(b). The results of these calculations are shown in Fig. 8, where the ITB and non-ITB regions are the same as in Fig. 3. As with the electron temperature profiles (compare with Fig. 3),  $R/L_{Ti}$  values exhibit a similar downward trend at or near the ITB foot location. It should be noted that in these TRANSP simulations the coefficient  $\kappa$  in  $\chi_i$  formulation equals 8-10 during L-mode and decreases down to 2-4 during H-mode. For certain discharges, especially the ones that developed an ITB, this coefficient drops down to and even below 1. This occurs primarily during the ITB phase of the discharge. Varying certain plasma parameters like impurity content or  $T_e$  within experimental errors changes the energy equilibration term,  $Q_{ie}$ . This changes the values of  $\kappa$  and as a result of  $\chi_i$  necessary to produce

such ion temperature that would lead to having the calculated neutron rate match the

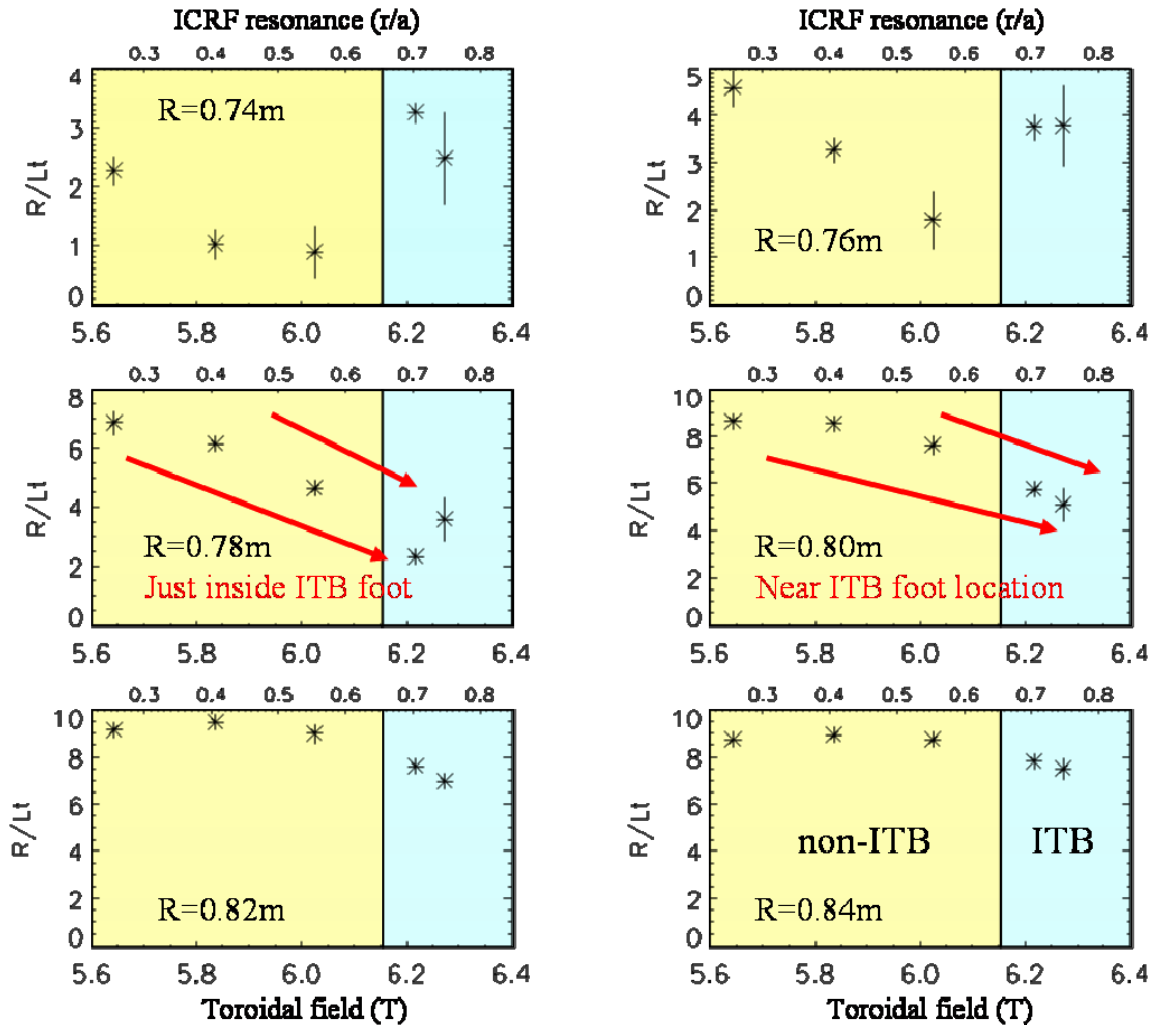


Figure 8 (Color online).

$R/L_T$  for the ion temperature calculated at the indicated radial positions shown on Fig. 1(b). All values are calculated during H-mode (pre-ITB) phase. Ion temperature profiles are calculated by TRANSP and are shown in Fig. 7. The  $r/a$  position of the ICRF resonance is shown on the upper axis. Left region on each plot corresponds to non-ITB discharges, while right region contains discharges that developed ITBs. As with the electron temperature there is a downward trend for  $R/L_T$  at positions at or near ITB foot location.

measured one. The resultant coefficient of proportionality,  $\kappa$  equals 1.5-2.5 during the pre-ITB phase in the H-modes for the discharges that developed ITBs. It is important to emphasize that as a result of these sensitivity studies the overall trends for  $T_i$  being broader than  $T_e$  and the region of reduced gradient of  $T_i$  moving outward with the ICRF power

deposition profile persist. More detailed  $T_i$  profiles measurements will become available in the next experimental campaign.

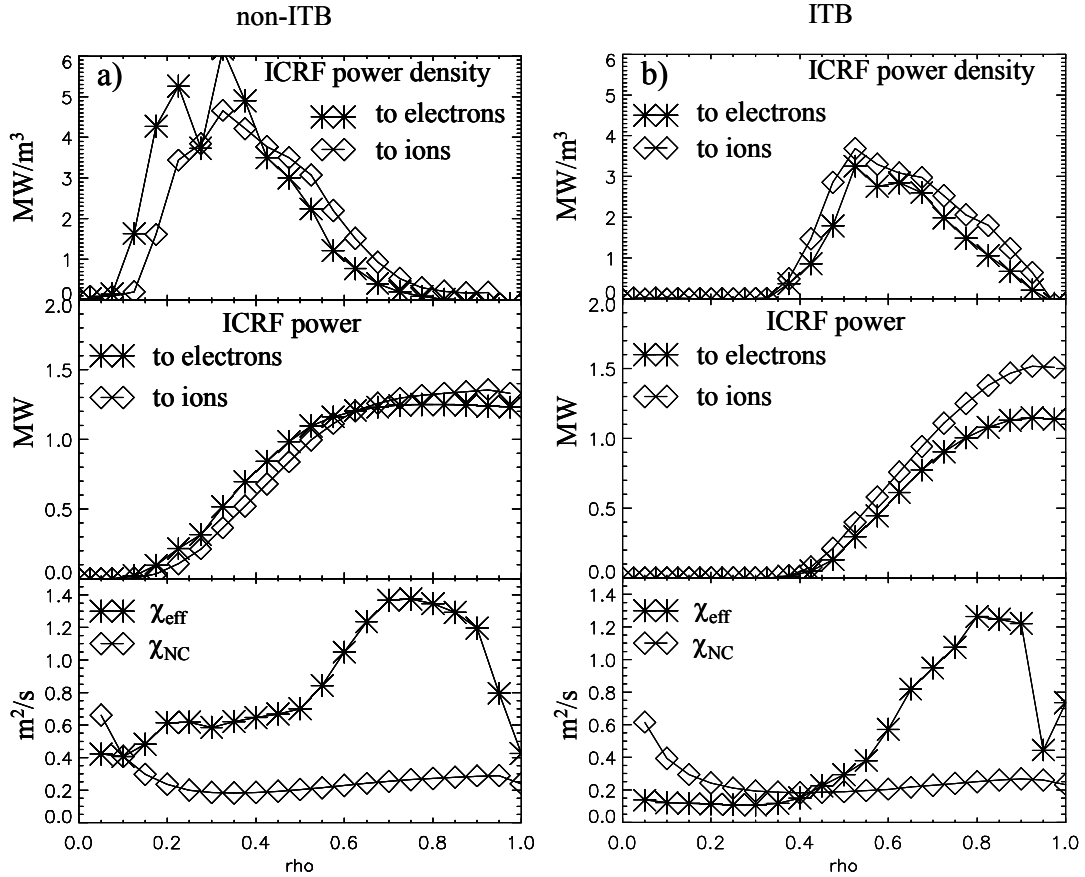


Figure 9. ICRF radial power density profiles (upper plots), radial total power distribution (middle plots) and thermal transport coefficients (lower plots) as calculated by TRANSP for a) non-ITB and b) ITB discharges. There is approximately the same amount of ICRF power going to ions (diamonds) and electrons (asterisks) in the non-ITB discharge. There is ~50% more ICRF power going to ions than to electrons in the ITB discharge. Effective thermal conductivity (asterisks,  $\chi_{eff} = (\chi_i n_i \nabla T_i + \chi_e n_e \nabla T_e) / (n_i \nabla T_i + n_e \nabla T_e)$ ) is significantly higher than neoclassical values (diamonds) across the whole plasma volume during the H-mode phase in the non-ITB discharge (a). However, it reaches neoclassical values inside the ITB foot during the ITB phase (b).

TRANSP calculations for the abovementioned discharges show that the ion minority tail temperature does not exceed 5 keV, and the tail density for off-axis heating cases is typically 5%. This result is in good agreement with the experimental measurements [37] from Alcator C for similar plasma parameters. At this rather low temperature, hydrogen minority ions from the tail of the distribution caused by ICRF tend to equilibrate with both deuterium

ions and electrons. Fig. 9 shows the radial density profiles of the ICRF power, total power distribution between ions and electrons and thermal diffusivities for some of the analyzed non-ITB (Fig. 9a) and ITB (Fig. 9b) discharges. The density and temperature profiles adopted on these TRANSP analyses are shown in Fig. 7 and Fig. 1b. Upper plots in Fig. 9 show density profiles of ICRF power going to deuterium ions (diamonds) and electrons (asterisks), while middle plots depict total ICRF power distribution between ions (diamonds) and electrons (asterisks). From this picture it can be seen that approximately the same amount of ICRF minority heating power goes to ions and electrons in the discharges that do not develop ITBs. However, there is approximately 50% more power going to deuterium ions than to electrons in the discharges that develop ITBs. There is enough heating power to the ions and ion thermal transport is sufficiently low, at least locally, to create small deviations of ion temperature from the electron temperature, which can be seen in Fig 7. Off-axis heating results in a local flattening of the temperature profiles, which in turn can decrease the drive for the ITG modes. TRANSP calculations of the effective

$(\chi_{eff} = (\chi_i n_i \nabla T_i + \chi_e n_e \nabla T_e) / (n_i \nabla T_i + n_e \nabla T_e))$ , asterisks) and neoclassical ( $\chi_{NC}$ , diamonds)

thermal conductivities are shown in the lower plots.  $\chi_{eff}$  remains well above neoclassical values across the whole plasma volume for the non-ITB discharge, while during the ITB it approaches neoclassical values inside the ITB foot, which is at  $r/a = 0.5$ . The convection flow term is not included in  $\chi_{eff}$  calculations and these profiles are consistent with previous C-Mod results [4, 6]. This drop in  $\chi_{eff}$  inside the barrier foot to near neo-classical levels suggests once again that this ITB is an energy barrier as well.

## 5. Gyrokinetic calculations.

In order to assess the effect of the observed broadening of the temperature profile on the diffusion caused by the microturbulent modes, stability analysis using the linear

gyrokinetic code GS2 [38, 39] was performed. Calculations were carried out on the MIT Plasma Science and Fusion Center Theory Group parallel computational cluster Marshall. In this analysis, growth rate profiles of ITG/TEM/ETG modes were computed based on the TRANSP calculations for the discharges from the magnetic field scan experiments.

Calculations were performed in non-adiabatic electrostatic mode using four plasma species: electrons, deuterium, minority hydrogen, and boron as an impurity. In all cases stability analysis is done at the ITB onset time.

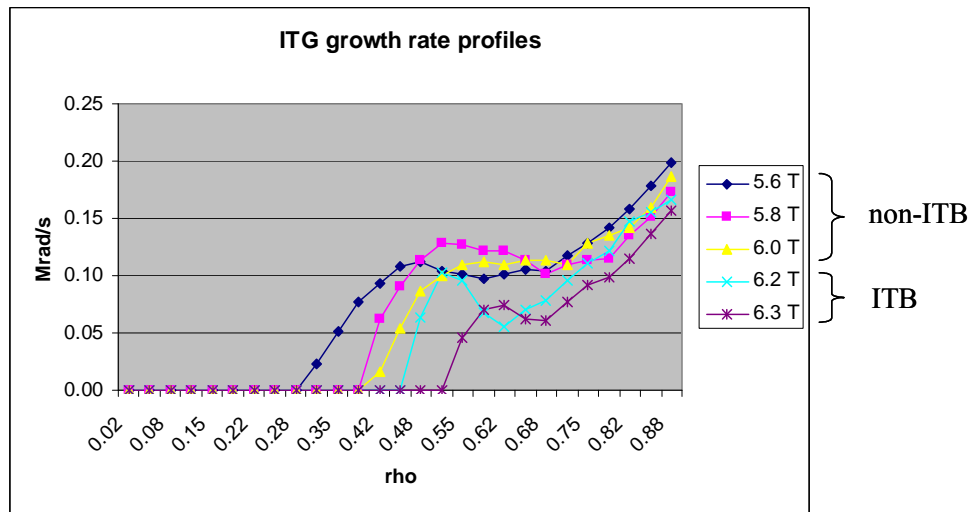


Figure 10 (Color online).

Linear ITG growth rate profiles calculated at ITB onset times. Higher field corresponds to more off-axis heating. There is no ITG turbulence in the core plasma region. Region of stability to ITG modes gets wider as the ICRF resonance is moved outward by changing the magnetic field. For ITB discharges it extends radially to approximately the location of ITB foot. ITG growth rates are systematically lower for the discharges that developed ITBs.

Fig. 10 depicts ITG growth rate profiles for the discharges from Fig. 7. These modes are characterized by normalized wave vectors,  $0.1 \leq k_{\perp} \rho_i \leq 1$ , where  $k_{\perp}$  is the wave vector component perpendicular to the magnetic field line. In the mode's spectrum analysis we found that the growth rate of ITG modes peaks at  $k_{\perp} \rho_i \sim 0.3-0.4$  ( $\rho_i = \sqrt{T_i / m_i} / \omega_{ci}$ ) for all of the analyzed discharges. Fig. 11(a) shows a typical ITG spectrum for an outer plasma region, which is strongly unstable to ITG modes. Profiles shown in Fig. 10 correspond to different

shots with different magnetic fields. In this particular case, lower field corresponds to on-axis heating, while higher field corresponds to more off-axis heating as can be seen from Fig. 7. Fig. 10 shows that ITG modes are suppressed in the core plasma region and the region of stability to ITG modes gets wider as the ICRF resonance is moved outward. This analysis also suggests that the growth rate of ITG modes is systematically lower for the discharges that developed ITBs than that of the non-ITB discharges. Moreover, the ITB foot is located at  $r/a \sim 0.5$ , approximately the location to which the stable region extends at a higher field. Fig. 10 also suggests that one should expect a slightly broader ITB for 6.3 T discharge than for 6.2 T. However, electron density profiles as measured by Thomson scattering system do not have enough spatial resolution to make a conclusive statement for such similar discharges. The analysis of a broader dataset of C-Mod ITB discharges does not allow us to conclude that ITB foot is always located at exactly the position of the ICRF resonance either, since there are cases where the ITB is formed to the inside of the ICRF power deposition. Fig. 7d illustrates this effect to some extent.

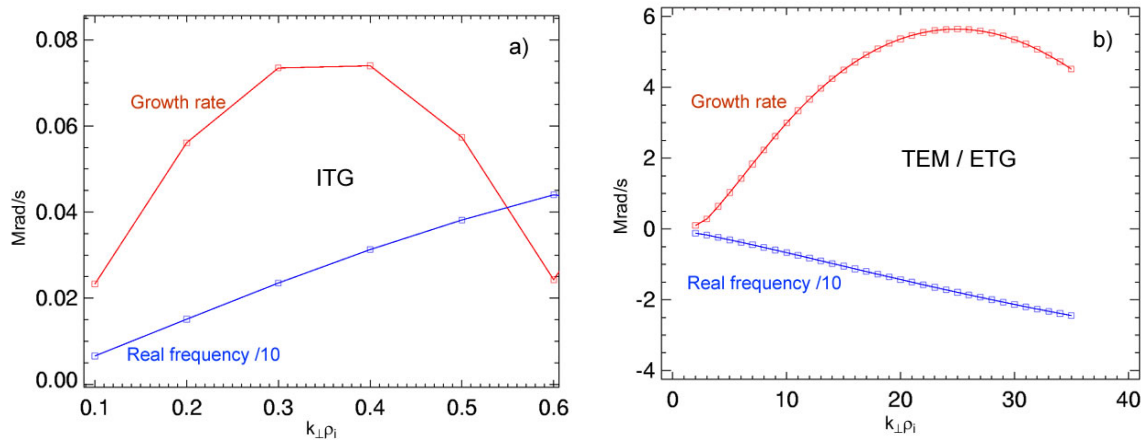


Figure 11 (Color online).

Linear growth rate and real frequency spectrum for a) ITG and b) TEM/ETG modes calculated at ITB onset time for a radial position just outside ITB. ITG mode spectrum peaks at  $k_{\perp}\rho_i \sim 0.3-0.4$ , while ETG mode spectrum usually peaks at  $k_{\perp}\rho_i \sim 25$  with a slight shift toward shorter wavelengths for positions closer to plasma edge. TEM range does not have distinct boundaries and corresponds to a longer wavelength part of the spectrum.

Figure 11(b) shows a typical TEM/ETG pre-ITB spectrum for a position just outside the ITB foot location. The spectrum for ETG modes usually peaks at  $k_{\perp}\rho_i \sim 25$  with a slight shift toward shorter wavelengths for radial positions closer to the plasma edge. The fastest growing ETG modes in our analysis usually have growth rates of 6-8 Mrads/s. In Fig. 11(b) no clear or distinct contribution from trapped electron modes can be seen in the longer wavelength part of the spectrum. Standard mixing length arguments imply that the nonlinear saturation of these instabilities occurs when non-linear damping becomes comparable to the linear growth rate. This leads to a scaling of particle and thermal transport coefficients of  $D, \chi \sim \Delta x^2 / \Delta t \sim \gamma / k_{\perp}^2$ , where  $\gamma, k_{\perp}$  are the growth rate and the perpendicular wave vector of

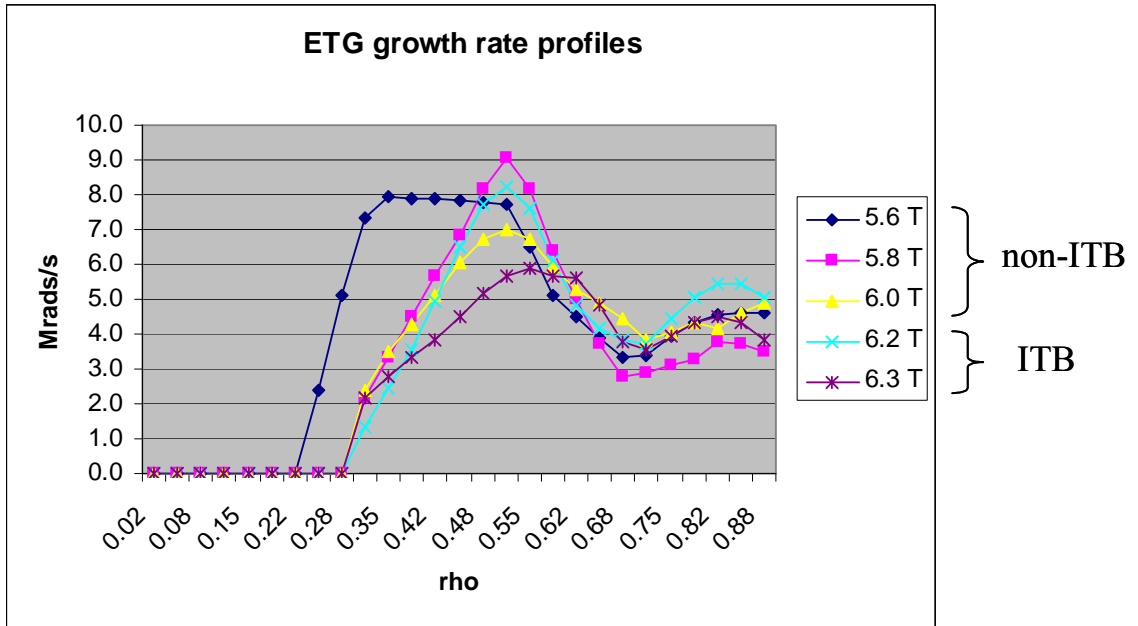


Figure 12 (Color online).

Linear ETG growth rate profiles calculated at ITB onset times. There is no clear difference between ETG growth rate profiles corresponding to ITB vs. non-ITB discharges.

the fastest growing mode. Comparison of growth rates and wave numbers of ITG and ETG modes leads to a conclusion that the contribution of ETG modes to the overall transport on C-Mod is negligible. Of course, ETG turbulence may be highly anisotropic [39], resulting in



transport levels much higher than mixing length estimates. Nevertheless, recent nonlinear ETG simulations that include ion dynamics show that ETG modes make only a small contribution to overall transport when ITG modes are unstable [41]. Further linear GS2 calculations do not reveal any difference between ETG growth rate profiles for ITB vs. non-ITB cases. Shown in Fig. 12 are the ETG growth rate profiles for the shots used in Fig. 10. Even though some variations in the profiles are observed it is not possible to derive any systematic trend or make a clear distinction between ITB and non-ITB cases in the way it can be done for ITG modes in Fig. 10. This suggests that the major difference in particle transport occurs due to suppression in ITG growth rates.

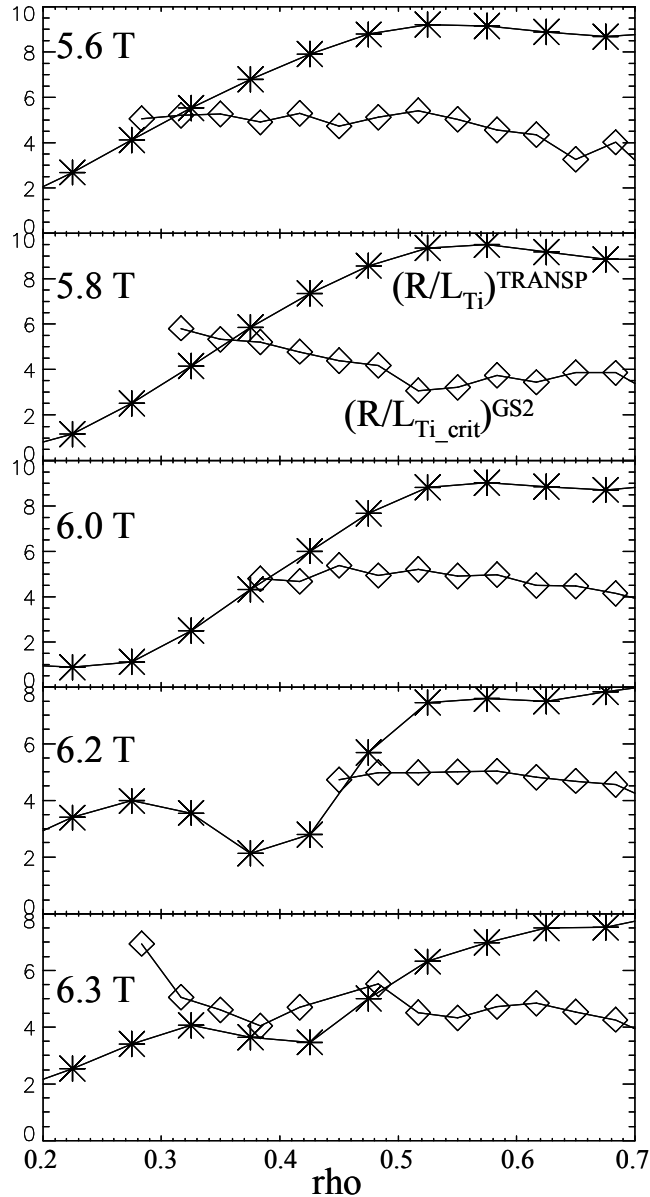


Figure 13.

$R/L_T$  for the ion temperature. Asterisks correspond to the  $R/L_{Ti}$  values derived for the ion temperature profiles calculated by TRANSP. Diamonds represent critical  $R/L_T$  values from linear GS2 analysis. The region of reduced gradient for which  $R/L_T < R/L_T^{crit}$  extends further out for the high field, or conversely off-axis heated discharges. The sawteeth inversion radius extends to  $r/a \sim 0.3$  for on-axis heated and to  $\sim 0.2$  for off-axis heated discharges.

It is not entirely clear what drives the transport in the central plasma region. In general, the turbulence stabilization depends on the competition of the driving forces such temperature and density gradients and stabilizing mechanisms such as magnetic shear  $\hat{s}$ ,  $q$ ,

$\nabla\beta$ , collisional effects etc. (see Refs. 32, 40 for more details and additional citations about the plasma physics underlying these effects). However, all the latter parameters are similar for ITB vs. non-ITB discharges and only a systematic change in the temperature gradient is observed as the ICRF resonance location is shifted radially. Fig. 13 shows  $R/L_{Ti}$  values derived for the ion temperature profiles calculated by TRANSP together with the critical gradient values estimated from linear GS2 analysis. It is seen that the region of reduced temperature gradients for which  $R/L_T < R/L_T^{crit}$  extends further out for the high field, or conversely off-axis heated discharges.

Stability analysis on Alcator C-Mod [18] and throughout the database on other machines [e.g., Ref. 42] shows that plasma core is generally stable to microturbulent drift modes to relatively large  $r/a$  values. It still remains to be explained why ITBs are not formed all the times at smaller radii and this question is beyond the scope of this paper. It is likely that some other transport driving mechanisms are at play in the inner part of the plasma that do not allow density peaking in the core region predicted to be stable to ITG modes. The potential candidate for C-Mod could be the transport induced by sawtooth oscillations. The sawteeth are definitely more pronounced and have larger inversion radius for on-axis heated discharges. For example, for the discharges shown in Fig. 7 the sawtooth inversion radius extends to  $r/a \sim .3$  for on-axis heating and to  $r/a \sim .2$  for off-axis heating scenarios. In all cases the ITB foot is located outside the sawtooth inversion radius. So, for ITB discharges the sawtooth inversion radius is smaller and the region of ITG stability is wider as can be seen from Fig. 10 and 13. This means that the gap between sawtoothing and ITG-unstable region is wider for ITB than for non-ITB discharges. GS2 analysis reveals that increasing temperature gradients by  $\sim 50-100\%$ , which is not unreasonable for the region just outside the sawtooth inversion radius, helps close this gap for on-axis heated discharges. This might help explain the fact that ITBs on C-Mod are obtained in the discharges with off-axis ICRF heating.

## 6. Discussion and conclusions.

Several sets of experiments have been performed on the Alcator C-Mod tokamak to test the hypothesis that the ITB formation in off-axis ICRF heated steady-state EDA H-mode plasmas can be explained within the paradigm of marginal stability to ITG modes. Experimental measurements of plasma temperature reveal that both ion and electron temperature profiles flatten in the region of ITB formation as the ICRF resonance location is moved outward, either by changing the toroidal magnetic field or by changing the ICRF setup. TRANSP simulations of the ion temperature profile are in good agreement with this experimentally observed trend, with the absolute deviation between ion and electron temperatures being small. Linear gyrokinetic GS2 calculations of the C-Mod H-mode plasmas at the ITB onset time suggest that TEM/ETG turbulence is negligible compared to that driven by ITG modes in the early phase of ITB. Moreover, these calculations do not reveal any systematic difference in the TEM/ETG modes' growth rate profiles between ITB and non-ITB discharges. Analysis of ITG growth rates, on the contrary, shows that the region of stability to these modes gets wider as the ICRF resonance location is moved outward. The turbulence is suppressed in the core plasma region before an ITB formation, which is in qualitative agreement with experimental transport calculations. Furthermore, for ITB discharges the region of stability to ITG modes radially extends approximately to the position of the ITB foot later in the discharge. Overall this suggests that suppressing ITG turbulence is a dominant factor in the triggering mechanism for off-axis ICRF heated ITBs on Alcator C-Mod. Comparison of the sawtooth inversion radius and region of ITG stability might help explain the fact that ITBs are formed in off-axis heated discharges. Linear gyrokinetic analysis seems to support this picture.

Improved measurements of ion temperature and plasma rotation profiles are expected in the new operation campaign. Extensive nonlinear gyrokinetic calculations will be

performed to calculate turbulence driven particle flux in order to compare it to the neoclassical pinch. Preliminary results of such nonlinear analysis show that this flux is close in magnitude to the Ware pinch, which is in line with the previous results [17] and overall picture of ITB formation on C-Mod. Also the dependence of the turbulence level on the temperature gradients for the C-Mod H-mode plasmas will be investigated.

### **Acknowledgements.**

The authors would like to thank the Alcator C-Mod engineering and technical staff for providing regular and reliable experimental operation.

This work was supported by Department of Energy Cooperative Agreement DE-FC02-99ER54512.

## References

- [1] Rice J E *et al.*, Nucl. Fusion **41**, 277 (2001).
- [2] Fiore C L *et al.*, Phys. Plasmas **8**, 2023 (2001).
- [3] Wukitch S J *et al.*, Phys. Plasmas **9**, 2149 (2002).
- [4] Rice J E *et al.*, Nucl. Fusion **42**, 510 (2002).
- [5] Ernst D R *et al.*, Phys. Plasmas **11**, 2637 (2004).
- [6] Fiore C L *et al.*, Phys. Plasmas **11**, 2480 (2004).
- [7] Waltz R E *et al.*, Phys. Plasmas **1**, 2229 (1994).
- [8] Mazzucato E *et al.*, Phys. Rev. Lett. **77**, 3145 (1996).
- [9] Burrell K H, Phys. Plasmas **4**, 1499 (1997).
- [10] Gruber O *et al.*, Phys. Rev. Lett. **83**, 1787 (1999).
- [11] Strait E J *et al.*, Phys. Rev. Lett. **75**, 4421 (1995).
- [12] Chan V S *et al.*, Nucl. Fusion **40**, 1137 (2000).
- [13] JET team (prepared by A C C Sips), Nucl. Fusion **41**, 1559 (2001).
- [14] Levinton F M *et al.*, Phys. Rev. Lett. **75**, 4417 (1995).
- [15] Bonoli P T *et al.*, in *Proc. 14<sup>th</sup> Topical Conf. on Radio-Frequency Power in Plasmas*, Oxnard, CA (APS, Woodbury, New York, 2001), p. 178.
- [16] Rice J E *et al.*, Nucl. Fusion **43**, 781 (2003).
- [17] Ernst D R *et al.*, in *Proc. 20<sup>th</sup> IAEA Fusion Energy Conf.*, Vilamoura, Portugal, November 1-6, 2004.
- [18] Redi M H *et al.*, Phys. Plasmas **12**, 072519 (2005).
- [19] Ernst D R *et al.*, in *Proc. 21<sup>st</sup> IAEA Fusion Energy Conf.*, Chengdu, China, October 16-21, 2006.
- [20] Hutchinson I H *et al.*, Phys. Plasmas **1**, 1511 (1994).
- [21] Takase Y *et al.*, *14<sup>th</sup> Symp. on Fusion Engineering*, San Diego, 1992 (IEEE, Piscataway, NJ, 1992), p. 118.
- [22] Schilling G *et al.*, *13<sup>th</sup> Topical Conf. on Radio Frequency Power in Plasmas*, Annapolis, 1999 (Melville, NY: AIP), Vol. 485, p. 429.
- [23] O'Shea P J, Hubbard A E, and Alcator C-Mod group, *Proc. 9<sup>th</sup> Joint Workshop on ECE and ECH, Borrero Springs, CA*, January 23-26, 1995 (World Scientific, New Jersey, 1995), pp. 393-401.
- [24] Taylor G *et al.*, *Bull. Am. Phys. Soc.*, **43**, 1821 (1998).
- [25] Heard J W *et al.*, *Rev. Sci. Instrum.* **70**, 1011 (1999).
- [26] Hughes J W *et al.*, *Rev. Sci. Instrum.* **74**, 1667 (2003).
- [27] Hughes J W *et al.*, *Rev. Sci. Instrum.* **72**, 1107 (2001).
- [28] Irby J H *et al.*, *Rev. Sci. Instrum.* **59**, 1568 (1988).
- [29] Marmor E S *et al.*, Nucl. Fusion **22**, 1567 (1982).
- [30] Rice J E and Marmor E S, *Rev. Sci. Instrum.* **66**, 752 (1995).
- [31] Fiore C L and Boivin R L, *Rev. Sci. Instrum.* **66**, 045 (1995).
- [32] Horton W, *Rev. Mod. Phys.* **71**, 735 (1999).
- [33] Tang W M *et al.*, *Phys. Fluids* **23**, 3715 (1986).
- [34] Hawryluk R J, in *Physics of Plasmas Close to Thermonuclear Conditions*, edited by B Coppi, G G Leotta, D Pfirsch, R Pozzoli, and E Sindoni (Pergamon, Oxford, 1980), Vol. 1, p. 19.
- [35] Chang C S and Hinton F L, *Phys. Fluids* **25**, 1493 (1982).
- [36] Brambilla M, *Plasma Phys. Cont. Fusion* **41**, 1 (1999).
- [37] Shepard T D *et al.*, *Phys. Fluids B* **3**, 1657 (1991).
- [38] Kotschenreuther M *et al.*, *Comput. Phys. Commun.* **88**, 128 (1995).
- [39] Dorland W *et al.*, *Phys. Rev. Lett.* **85**, 5579 (2000).
- [40] Wesson J A, *Tokamaks* (Oxford University Press, New York, NY, 1997).
- [41] Candy J and Waltz R E, in *Proc. 21<sup>st</sup> IAEA Fusion Energy Conf.*, Chengdu, China, October 16-21, 2006.
- [42] Romanelli M, Bourdelle C, and Dorland W, *Phys. Plasmas* **11**, 3845 (2004).